

Edge effects in elastic bulging

Félix Benoist, Finn Box, Alain Goriely *

Mathematical Institute, University of Oxford, United Kingdom

ABSTRACT

Elastic bulging occurs when an elastic material deforms through a small opening in a rigid boundary. This problem is complementary to the indentation problem where displacement is applied to a small part of an elastic material. Understanding bulging is crucial in a number of applications related to swelling such as the deformation of the brain following a decompressive craniectomy. In particular, it is known that large stresses develop close to the opening leading to potential material damage. To alleviate this problem, it is conceivable to modify the shape of the edge to reduce stress increases. Here, we study edge effects during planar bulging and show how an opening should be shaped to remove stress singularities.

1. Introduction

After a traumatic brain injury, intracranial pressure may increase [1] and create long lasting brain damage unless it is quickly reduced. If the intracranial pressure remains too large for an extended period of time, a routine, but highly invasive, treatment is *decompressive craniectomy* [2] where part of the skull is surgically removed [3] to allow the brain to swell uninhibitedly, thereby relieving pressure [4–7]. This operation is controversial because it creates potential axonal damage and local tissue damage near the skull opening [8,9].

A potential solution to reduce stress build-up at the opening is to insert a toric joint between the skull and the brain, which has the consequence of curving the edge and the elastic material [10]. We investigate the mechanical consequences of the implementation of a toric joint by examining bulging through an opening and the effect of the opening edges on the stress and strain inside a bulging elastic material.

Whereas indentation is the deformation of an elastic material due to the displacement of a small part of its boundary, bulging is the deformation of an elastic material through the opening of a rigid boundary. Unlike the case of indentation that has been studied extensively [11], bulging has received little attention in the literature and was only recently introduced as a generic problem motivated by medical concerns [12].

Here, we consider the bulging of a (linearly) elastic half-plane. For small deformations and in a planar geometry, the exact solution is derived from the theory of contact mechanics and we can explicitly study the deformations resulting from a sharp-edge and a curved-edge opening.

1.1. Preliminaries

We consider an elastic half plane $\Omega = \{x \in \mathbb{R}, z > 0\}$ subjected to a distributed load from a curved lip at the boundary. Inside the domain, the deformation is described by a displacement field $\mathbf{u} = (u_x, u_z) : \Omega \rightarrow \mathbb{R}^2$ such that a point originally at $\mathbf{x} \in \Omega$ displaces to a point at $(\mathbf{x} + \mathbf{u}) \in \mathbb{R}^2$. The (infinitesimal) strain tensor \mathbf{E} is

$$\mathbf{E} = \frac{1}{2} (\nabla \mathbf{u} + (\nabla \mathbf{u})^T). \quad (1.1)$$

As shown in Fig. 1, the boundary $\Gamma = \partial\Omega$ is split into two subsets where the elastic material is either in contact (Γ_c) or traction free ($\Gamma_f = \Gamma \setminus \Gamma_c$). On Γ_c the vertical displacement of the elastic material is constrained such that $u_z(x, z) = u_0(x)$, where u_0 is directly related to the profile of the plate. Note that apart from the curved edges, the plate is flat and rigid so that $u_0 = \delta$ is constant. At the boundary Γ_f , outside of Γ_c , the material is traction free.

The material is assumed to be a compressible, isotropic, initially unstressed, and linearly elastic solid with Young's modulus E and Poisson's ratio ν . Let \mathbf{T} be the Cauchy stress tensor, then the constitutive relationship between stresses and strains [13] is

$$\mathbf{T} = \frac{E}{1+\nu} \left(\mathbf{E} + \frac{\nu}{1-2\nu} (\text{tr } \mathbf{E}) \mathbf{1} \right), \quad (1.2)$$

where $\mathbf{1}$ is the identity tensor.

For a given profile $u_0(x)$, the *bulging problem* consists in finding the displacement \mathbf{u} and the contact region Γ_c , such that

$$\text{div } \mathbf{T} = \mathbf{0}, \quad \mathbf{x} \in \Omega, \quad (1.3)$$

$$\mathbf{T} \mathbf{n} = \mathbf{0}, \quad (x, 0) \in \Gamma_f, \quad (1.4)$$

$$u_z(x) = u_0(x), \quad (x, 0) \in \Gamma_c, \quad (1.5)$$

* Corresponding author.

E-mail address: goriely@maths.ox.ac.uk (A. Goriely).

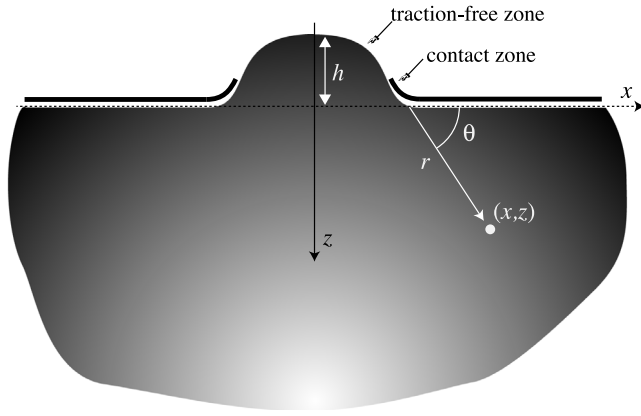


Fig. 1. An elastic material initially in a half-plane configuration is deformed by the vertical displacement of a rigid flat plate with curved edges. Doing so, it will develop a bulge. The contact zone and traction-free zone are indicated. Note that the point at which the material loses contact needs to be determined.

$$\mathbf{t} \cdot \mathbf{Tn} = 0, \quad (x, 0) \in \Gamma_c, \quad (1.6)$$

where \mathbf{n} (resp. \mathbf{t}) denotes the outward unit normal (resp. tangent) to Ω on Γ and the traction vector on Γ is given by \mathbf{Tn} . The last condition represents the frictionless constraint on the contact region.

1.2. The Cerruti–Flamant solution

Before we consider the case of a distributed load, we recall the classic Cerruti–Flamant solution for a half-space under a single normal point load P at the origin [14–16]. In this case, the radial stress is given

$$T_{rr} \equiv \mathbf{e}_r \cdot (\mathbf{T}\mathbf{e}_r) = -\frac{2P}{\pi} \frac{\sin \theta}{r}, \quad (1.7)$$

for a point located at $x = r \cos \theta$, $z = r \sin \theta$ (and $\mathbf{e}_r = (\cos \theta, \sin \theta)$) (see Fig. 1). This solution can be written in Cartesian coordinates as

$$T_{xx} = -\frac{2P}{\pi} \frac{x^2 z}{(x^2 + z^2)^2}, \quad (1.8)$$

$$T_{zz} = -\frac{2P}{\pi} \frac{z^3}{(x^2 + z^2)^2}, \quad (1.9)$$

$$T_{xz} = 0. \quad (1.10)$$

1.3. The Cerruti–Flamant solution as a Green’s function

Next, we assume that we have a distributed load. Since the contact is assumed to be frictionless, we have $p_x = 0$ which leads us to set $p(x) \equiv p_z(x)$, and we only consider symmetric loads i.e. $p(-x) = p(x) \forall x$. Then, the Cerruti–Flamant solution for the point load problem can be used as a Green’s function for a distributed normal force $p(x)dx$ on an element dx at each point on the surface.

$$T_{xx} = -\frac{2z}{\pi} \int_{-\infty}^{\infty} \frac{p(s)(x-s)^2}{((x-s)^2 + z^2)^2} ds, \quad (1.11)$$

$$T_{zz} = -\frac{2z^3}{\pi} \int_{-\infty}^{\infty} \frac{p(s)}{((x-s)^2 + z^2)^2} ds, \quad (1.12)$$

$$T_{xz} = -\frac{2z^2}{\pi} \int_{-\infty}^{\infty} \frac{p(s)(x-s)}{((x-s)^2 + z^2)^2} ds. \quad (1.13)$$

Using (1.1)–(1.2) at the surface $z = 0$, the displacement field $(u_x(x), u_z(x))$

$\equiv \mathbf{u}(x, 0)$ is related to the pressure field $p(x)$ as follows

$$\forall x \in \mathbb{R}, \quad \begin{cases} u_x(x) = \frac{B}{2} \int_S p(s) \operatorname{sgn}(x-s) ds \\ u_z(x) = -A \int_S p(s) \ln|x-s| ds, \end{cases} \quad (1.14)$$

where S is the subset of \mathbb{R} where contact is established ($S = \{x \in \mathbb{R} | (x, z) \in \Gamma_c\}$) and

$$A = \frac{2}{\pi} \frac{1-\nu^2}{E}, \quad B = \frac{(1+\nu)(1-2\nu)}{E}. \quad (1.15)$$

In the bulging problem, S is the union of two unbounded set $S = (-\infty, -a] \cup [a, \infty)$. Further since the derivative of the sign function can be expressed in the sense of distribution by Dirac’s delta: $d \operatorname{sgn}(x)/dx = 2\delta(x)$, differentiating (1.14) with respect to x leads to the following system of equations

$$\forall x \in \mathbb{R}, \quad \begin{cases} \frac{du_x}{dx} = Bp(x) \\ \frac{du_z}{dx} = -A \left(\int_{-\infty}^{-a} + \int_a^{\infty} \right) \frac{p(s)}{x-s} ds. \end{cases} \quad (1.16)$$

These relations directly connect the applied load to the surface displacement gradient. If the displacements are specified at the surface, the pressure needed to maintain this displacement is obtained by solving this system of equations. Once the pressure is known, the system (1.11)–(1.13) gives the stress at all points, from which the strains and displacements can be obtained. Notice that if the material is incompressible (i.e. $\nu = 1/2$), then $B = 0$.

1.4. Calculations of the pressure and the displacement

Since $u_z = u_0(x)$ is known in the contact zone, we have

$$\left(\int_{-\infty}^{-a} + \int_a^{\infty} \right) \frac{p(s)}{x-s} ds = -\frac{1}{A} \frac{du_0}{dx}(x) \equiv f(x), \quad |x| \geq a. \quad (1.17)$$

Mathematically, the problem is then to solve

$$\left(\int_{-\infty}^{-a} + \int_a^{\infty} \right) \frac{p(s)}{x-s} ds = f(x), \quad |x| \geq a, \quad (1.18)$$

for p . This is a singular integral equation of the first kind with a gap. This is not a standard problem for which solutions are readily available. In Appendix A, we use ideas from [17] to obtain the general homogeneous solutions (in the case where $f(x) = 0$) and, in Appendix B, we show how to obtain the solution for a particular $f(x)$ corresponding to a curved edge.

1.4.1. Sharp edges

We consider a uniform displacement δ in Γ_c . Therefore f vanishes identically and the pressure is given by the even homogeneous solution p_{even} of (1.18) as given in Appendix A.1:

$$p(s) = \frac{cE}{2} \frac{|s|}{\sqrt{s^2 - a^2}}, \quad |s| \geq a, \quad (1.19)$$

where $c > 0$ is an arbitrary dimensionless constant (note that the solution given in [12] contains typos that have been corrected here). From p , we find the derivative of the displacement in the bulging area i.e. outside of Γ_c :

$$\frac{du_z}{dx} = -2Ax \int_a^{\infty} \frac{p(s)}{x^2 - s^2} ds = Ax \frac{cE}{2} \frac{\pi}{\sqrt{a^2 - x^2}}, \quad |x| \leq a \quad (1.20)$$

and the vertical displacement is therefore

$$u_z(x) = \delta - c(1 - \nu^2) \sqrt{a^2 - x^2}, \quad |x| \leq a, \quad (1.21)$$

in which the constant c is related to both the height $h = c(1 - \nu^2)a$ and the area of the bulge $A_b = \pi ah/2$. We note that, remarkably, we recover the same expression as for the axisymmetric case for the bulging of a half-space [12] and that the shape of the bulge is an *ellipse* in two dimensions and an *ellipsoid of revolution* in three dimensions. The vertical displacement and the normal pressure at the surface are shown in Fig. 2 for $\delta = 0$. Note that the pressure is infinite at the edges.

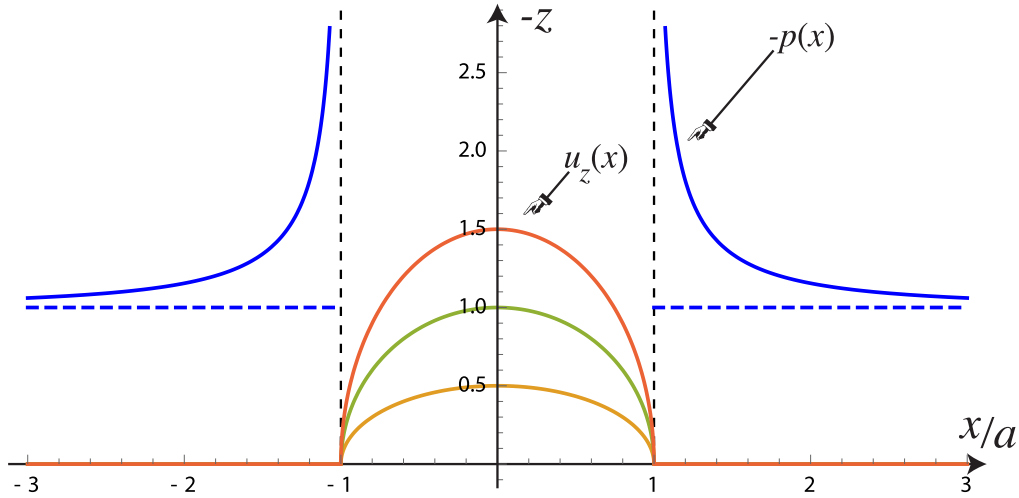


Fig. 2. Bulge solution with sharp edges. Here we show the pressure $p(x)$ (blue online), and vertical displacement $u_z(x)$ (in orange, green and red online) for increasing values of c . (For interpretation of the references to color in this figure legend, the reader is referred to the web version of this article.)

1.4.2. Experiments

Bulging experiments were performed by compressing confined elastic solids using a plate with a circular aperture. Under uniaxial compression, the soft solid bulged through the aperture permitting measurement of the axisymmetric deformation profile. The material properties and dimensions of the soft samples used in the experiments are detailed in Appendix C.

We compare the solution (1.21) with the experimentation profile for increasing bulging. For each experimental data set, we show the corresponding analytical solution with the same height h along the axis as shown in Fig. 3. We see that the analytical solution captures correctly most of the profile.

1.4.3. Curved edges

Next, we consider a plate with rounded parabolic edges defined in the interval $a \leq |x| \leq b$. In this case the non-homogeneous term in (1.18) is

$$f(x) = \begin{cases} 0, & |x| \geq b \\ \frac{x-b}{AR}, & a \leq x \leq b \\ \frac{x+b}{AR}, & -b \leq x \leq -a, \end{cases} \quad (1.22)$$

where R is the radius of curvature of the edge at $x = b$. The solution in this case is computed explicitly in Appendix B:

$$p(s) = -\frac{1}{\pi^2 AR} \left(|s| \ln \left| \frac{b^2 - 2a^2 + s^2 + 2\sqrt{(b^2 - a^2)(s^2 - a^2)}}{b^2 - s^2} \right| + b \operatorname{sgn}(s) \ln \left| \frac{b-s}{b+s} \frac{a^2 + bs - \sqrt{(b^2 - a^2)(s^2 - a^2)}}{a^2 - bs - \sqrt{(b^2 - a^2)(s^2 - a^2)}} \right| \right) \quad (1.23)$$

This expression has two parameters: b is given by the profile and a is the point at which the solid loses contact. This is a one-parameter family of solutions parametrized by a : for each value of a in the interval $(b-R, b]$, we obtain a solution with a given height at $x = 0$. Therefore, the parameter a plays the same role as the parameter c in the previous solution. As s tends to infinity, the pressure does not depend on the detailed profile of the edges. Hence, the two solutions can be related to each other and a satisfies the following equation

$$2\sqrt{1 - (a/b)^2} + \ln \left| \frac{1 - \sqrt{1 - (a/b)^2}}{1 + \sqrt{1 - (a/b)^2}} \right| = -\pi c(1 - v^2) \frac{R}{b}, \quad a \in (b-R, b]. \quad (1.24)$$

Notice that the parabolic approximation is only valid if $a > b - R$. The vertical displacement is calculated numerically and plotted with the normal pressure at the surface in Fig. 4 for $\delta = 0$. Notice that at the curved edges, the pressure is regularized.

In Fig. 5, we compare the resulting pressure in the case of straight and curved edges for $R/b = 0.2$. We notice that pressure in the curved-edge case is lower at equal height than it is in the sharp-edge case. For instance a bulge sticking to curved edges of radius $R/b = 0.2$ till $a = 0.9b$ is subject to the same pressure as a bulge out of a sharp-edge opening of height $h \approx 0.1a$ while being 1.6 times as high.

The displacements in the two cases are compared in Fig. 6. For the same height at 0, the profile of the bulge is almost identical in both cases. Experimental results are shown in Fig. 7.

We also note that the bulging area is slightly bigger in the curved-edge case since the material follows the edges before bulging out (for $R/b = 0.2$, the difference is less than 9%). This trend is recovered in the experiments where for a given aperture and swelling volume, the height of the profile for a curved-edge aperture is always larger than for the straight-edge case as shown in Fig. 8.

1.5. Calculations of the stresses

Since the normal surface pressure p is known for all values of x , the Cartesian components of the stress tensor \mathbf{T} can be calculated by using expression (1.11)–(1.13).

1.5.1. Sharp edges

First, we rescale the variables through $\bar{\xi} = \xi/a$ for each variables s , x and z . Moreover we introduce the new variables X, Y and ρ in which the expressions for T_{ij} are easily expressed:

$$\begin{cases} X = 1 + \bar{z}^2 - \bar{x}^2 \\ Y = 2\bar{x}\bar{z} \end{cases} \quad \text{and} \quad \rho = \sqrt{X^2 + Y^2}. \quad (1.25)$$

Finally, setting $E' = \frac{c}{2\sqrt{2}}E$ we obtain the following expressions for $x \geq 0$ and $z \geq 0$:

$$\begin{cases} \frac{T_{xx}}{E'} = -\frac{1}{\rho} \left(\bar{x}\sqrt{\rho-X} + \bar{z}\sqrt{\rho+X} \right) + \frac{\bar{z}}{\rho^3} \left(Y\sqrt{\rho-X} - X\sqrt{\rho+X} \right) \\ \frac{T_{xz}}{E'} = \frac{\bar{z}}{\rho^3} \left(X\sqrt{\rho-X} + Y\sqrt{\rho+X} \right) \\ \frac{T_{zz}}{E'} = -\frac{1}{\rho} \left(\bar{x}\sqrt{\rho-X} + \bar{z}\sqrt{\rho+X} \right) - \frac{\bar{z}}{\rho^3} \left(Y\sqrt{\rho-X} - X\sqrt{\rho+X} \right). \end{cases} \quad (1.26)$$

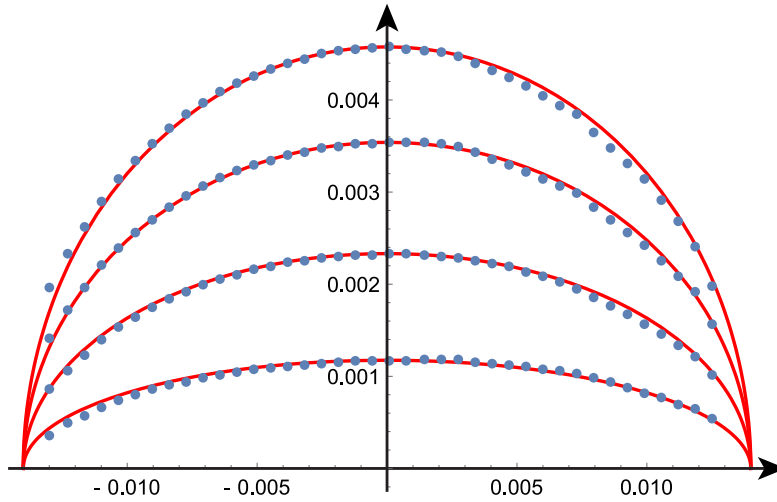


Fig. 3. Bulge solution with straight edges. Comparison between the analytical solution and experimental bulging (parameters given in [Appendix](#), all values on the axes are in meters). Note that the analytical solution uses an aperture of $a = 0.014$ m rather than the aperture of $a = 0.015$ m used in the experiment as it provides a better fit to the data. This small discrepancy may be due to a small bending of the sample at the straight edge. The experimental data can be found in the supplemental material file (ExpData_Fig3.csv).

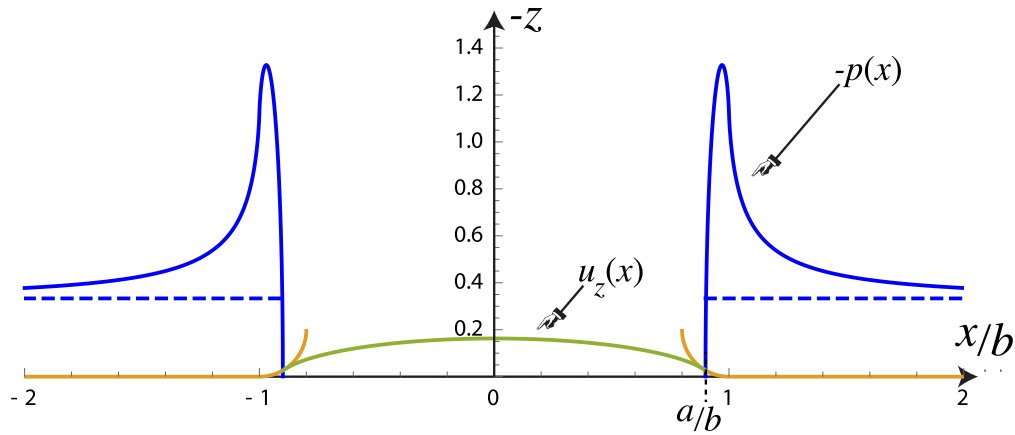


Fig. 4. Bulge solution with curved edges. Here we show the pressure $p(x)$ (blue online), and vertical displacement $u_z(x)$ (green online) for a given parabolic profile $u_0(x)$ (orange online) for $R/b = 0.2$. The solid loses contact at $a/b = 0.9$. (For interpretation of the references to color in this figure legend, the reader is referred to the web version of this article.)

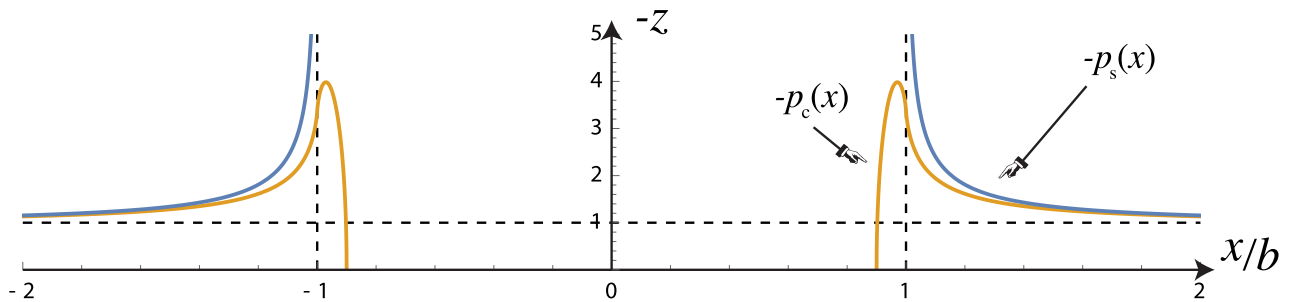


Fig. 5. Comparison of the pressure generated by a straight edge, p_s (blue online) with the pressure generated with a curved edge p_c (orange online). The singularity for the straight-edge case is placed at b and $a/b = 0.9$. (For interpretation of the references to color in this figure legend, the reader is referred to the web version of this article.)

We note that in the far field (for large value of x), the stress tensors at the boundary ($z = 0$) tends to a hydrostatic field with $T_{xx} = T_{zz} = -cE/2$, necessary to maintain a uniform displacement of the plate. Close to the contact, we are specifically interested in the shear stress T_{xz} as a potential indicator of damage. In [Fig. 9](#), we show the shear stress with respect to the reference configuration. Close to the edges, we observe

typical drop-like regions of damage that have been experimentally studied in [\[10\]](#). Their shape is approximated by using the right-side polar representation ($x \geq 0$):

$$\begin{cases} x = a + r \cos \theta \\ z = r \sin \theta. \end{cases} \quad (1.27)$$

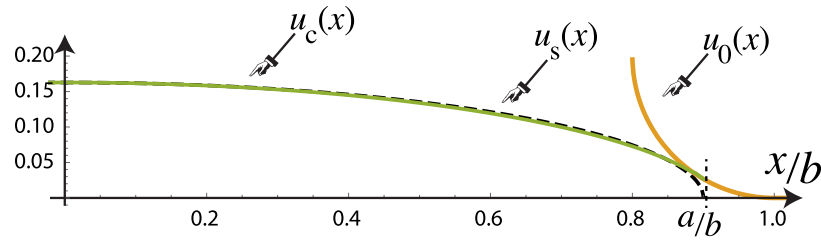


Fig. 6. Comparison of the displacement generated by a sharp edge, u_s (dashed) with the displacement u_c (solid green online) generated by a curved edge $u_0(x)$ (orange online). Here $a/b = 0.9$ and $R/b = 0.2$. The values are chosen so that $u_s(0) = u_c(0)$. We conclude that the displacements for a curved edge are very close to those generated by a sharp edge of a slightly smaller radius. (For interpretation of the references to color in this figure legend, the reader is referred to the web version of this article.)

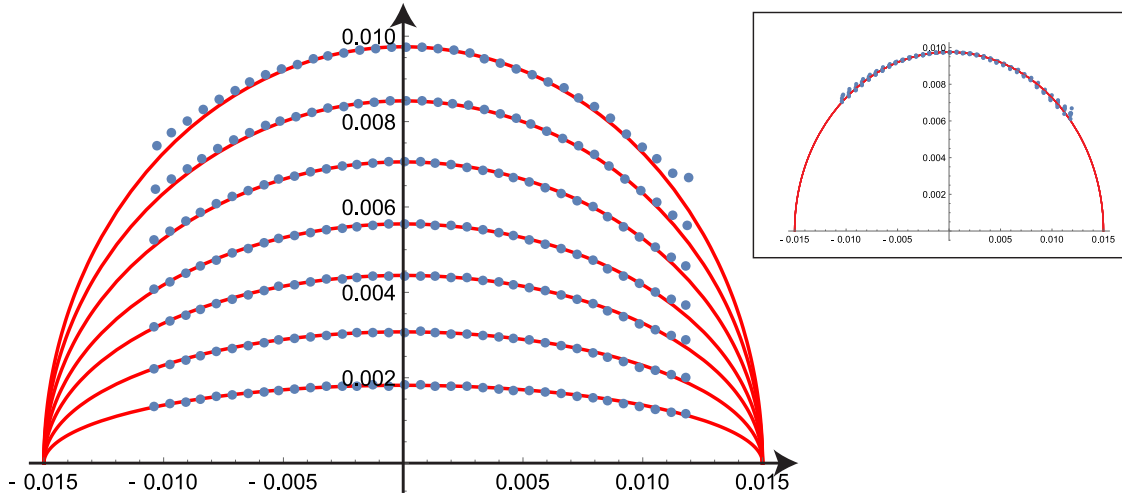


Fig. 7. Bulge solution with curved edges. Comparison between the analytical solution and experimental bulging (parameters given in Appendix, all values on the axes are in meters). Note that since the profile with straight and curved edges are almost identical, the analytical solution shown here is the simpler straight edge case.

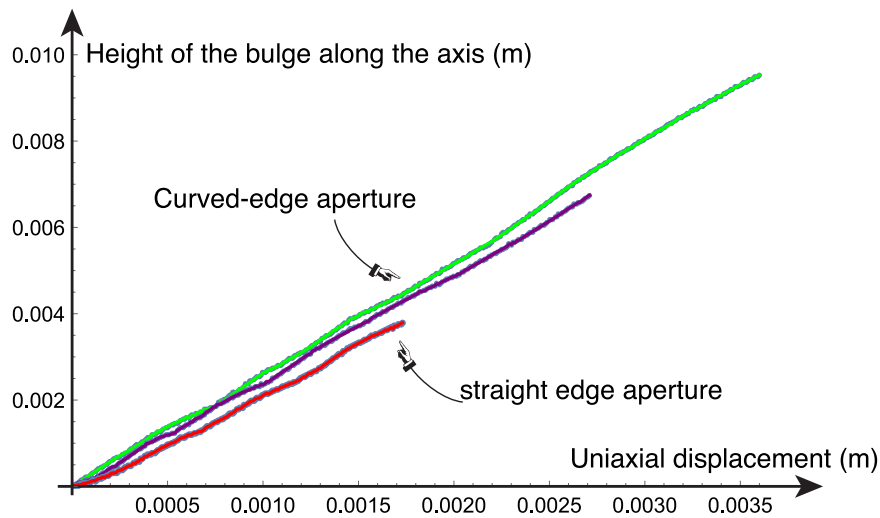


Fig. 8. Profile height as a function of the uniaxial compression (corresponding to an increasing swelling volume) for curved-edge and straight-edge apertures. The experimental data can be found in the supplemental material file (ExpData_Fig8.csv).

For $r \ll a$, shear stress is approximated at the lowest order in \bar{r} by

$$\sigma_{xz}^{\text{app}} = \frac{cE}{8} \frac{\sin \theta}{\sqrt{f}} \left(\cos \theta \sqrt{1 + \cos \theta} - \sin \theta \sqrt{1 - \cos \theta} \right). \quad (1.28)$$

We recover the well-known scaling law $r^{-1/2}$ of stress around the singularity [18].

Let τ_{crit} be the critical value of shear stress past which damage occurs. We introduce the dimensionless parameter $K = cE/8\tau_{\text{crit}}$ to measure the extent of the damage zone. The shape of a damage drop is then defined by the polar curve

$$\bar{r}(\theta) = K^2 \sin^2 \theta (1 + \cos 3\theta), \quad 0 \leq \theta \leq \pi, \quad (1.29)$$

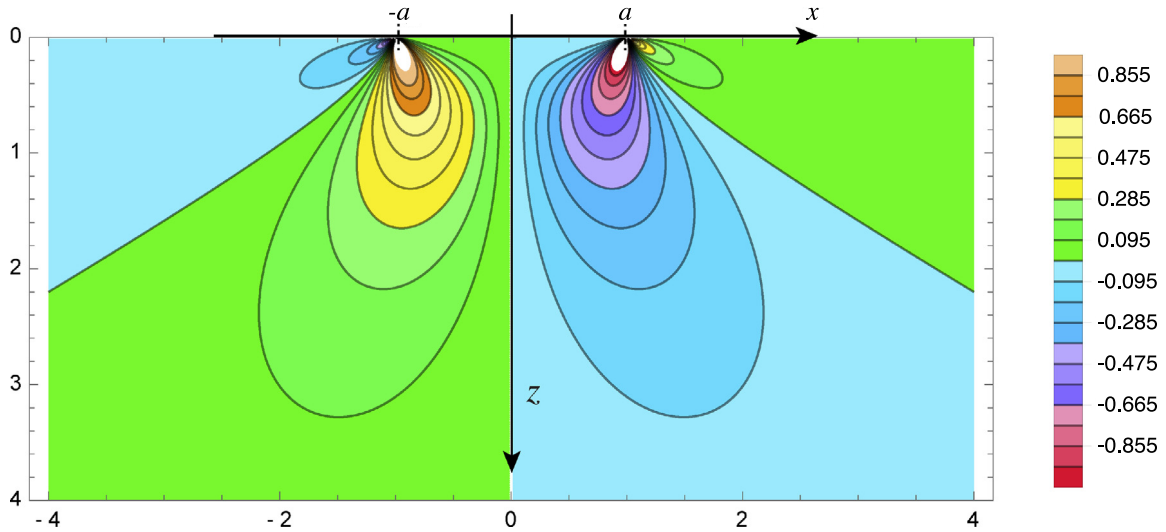


Fig. 9. Contour plot of the shear stress T_{xz} in the flat case for $a = 1$ and $cE = 1$.

shown in Fig. 10. The two damage drops are inclined with angles

$$\alpha_{\pm} = 2 \arctan \left(\frac{1}{2} \sqrt{\frac{1}{3} (13 \pm \sqrt{145})} \right) \approx 111^\circ \text{ and } 32^\circ \quad (1.30)$$

Their area are

$$\begin{aligned} A_+ &= \frac{3(280\pi + 243\sqrt{3})}{1120} a^2 K^4 \approx 3.48 a^2 K^4 \\ A_- &= \frac{3(140\pi - 243\sqrt{3})}{1120} a^2 K^4 \approx 5.07 \times 10^{-2} a^2 K^4. \end{aligned} \quad (1.31)$$

The relative growth of the total area of the four drops compared with the area of the bulge is given by

$$2 \frac{A_+ + A_-}{A_b} = \frac{9}{2^{13}} \frac{c^3}{1 - \nu^2} \left(\frac{E}{\tau_{\text{crit}}} \right)^4 \approx 1.10 \times 10^{-3} \frac{c^3}{1 - \nu^2} \left(\frac{E}{\tau_{\text{crit}}} \right)^4. \quad (1.32)$$

At a given τ_{crit} , the drops area increase as c^3 compared to the bulge area. Thus, we expect these damage drops to grow quickly after initiation. For instance, the largest bulge shown in Fig. 2 has a dimensionless height $h/a = c(1 - \nu^2) = 1.5$, for $\nu = 0.3$ and $\tau_{\text{crit}} = E/2$. Its area is almost 9% of the total bulge area.

1.5.2. Curved edges

For curved edges, the shear stress is calculated numerically (Fig. 11). We note that for $a/b = 0.9$, the damage drops are so small that the smaller one is no longer visible and can be neglected. Therefore, we restrict our attention to the bigger damage drops.

The big damage drops are plotted for increasing values of a in Fig. 12. Furthermore their areas A_+ are numerically evaluated and fitted by a polynomial. It is worth noticing that even the big damage drop is no longer visible for $a/b < 0.8$ at $K = 1$.

1.6. Stretching

Another possible indicator of damage is the stretches of fibers contained within a material (axons in the case of the brain). So far, only stress-related damages have been studied. Nevertheless intense stretching may also damage axons. In order to study the stretches, we need to calculate the displacement field everywhere in the half space. The strain and stress tensors respectively noted with components e_{ij} and T_{ij} are related by

$$\mathbf{E} = \frac{1 + \nu}{E} \mathbf{T} - \frac{\nu}{E} (\text{tr } \mathbf{T}) \mathbf{1}. \quad (1.33)$$

Although we have been working under the assumption that the material is homogeneous and isotropic, it is only an approximation since brains are made of axons. In the case of bulging, axons are likely to lean towards the bulging direction which is vertical in the geometry studied here. Thus, in order to study the damage caused to axons by stretching, we further investigate the vertical stretch $\lambda_z = 1 + \partial_z u_z$ which is given by

$$\lambda_z = 1 + \frac{T_{zz} - \nu T_{xx}}{E}. \quad (1.34)$$

1.6.1. Sharp edges

In the sharp-edge case, the vertical stretch is given by

$$\begin{aligned} \lambda_z = 1 - \frac{c(1 - \nu)}{2\sqrt{2}\rho} \left(\bar{x}\sqrt{\rho - X} + \bar{z}\sqrt{\rho + X} \right) \\ - \frac{c(1 + \nu)\bar{z}}{2\sqrt{2}\rho^3} \left(Y\sqrt{\rho - X} - X\sqrt{\rho + X} \right). \end{aligned} \quad (1.35)$$

The vertical strain $e_z = \lambda_z - 1$ is plotted in Fig. 13.

As expected, the stretch takes minimal values close to the edges with a singularity in $r^{-1/2}$ as for shear stress. Moreover, the stretch takes maximal values on the symmetry line $x = 0$ at the point $z_{\text{max}} = a\sqrt{2\nu/(3 + \nu)}$. In the incompressible limit $\nu \rightarrow 1/2$ at which the stretch is maximal, since $c = \frac{h}{a(1 - \nu^2)}$ it is written on the symmetry line :

$$\lambda_z(0, z) = 1 + \frac{h}{3a} \frac{z}{a^{3/2}} \frac{2a^2 - z^2}{(a^2 + z^2)^{3/2}}, \quad (1.36)$$

with the maximal value

$$\lambda_{\text{max}} = 1 + \frac{4\sqrt{2}}{27} \frac{h}{a}. \quad (1.37)$$

1.6.2. Curved edges

In the case of curved edges, the vertical strain is numerically calculated and plotted in Fig. 14 in both cases for comparison. Unlike the shear stress, for $a/b = 0.9$, damage areas related to vertical stretching are much larger with a curved-edge.

In the case of a curved edge, we find that in order to prevent large stretching along the axis so that it is comparable to the sharp-edge case, the ratio a/b must be larger than 0.95 (Fig. 15). Since, we know that in the particular case where $R/b = 0.2$, the ratio a/b is about 0.9 for small bulges, we see that the radius of curvature must further decrease in order to reduce the fiber stretch.

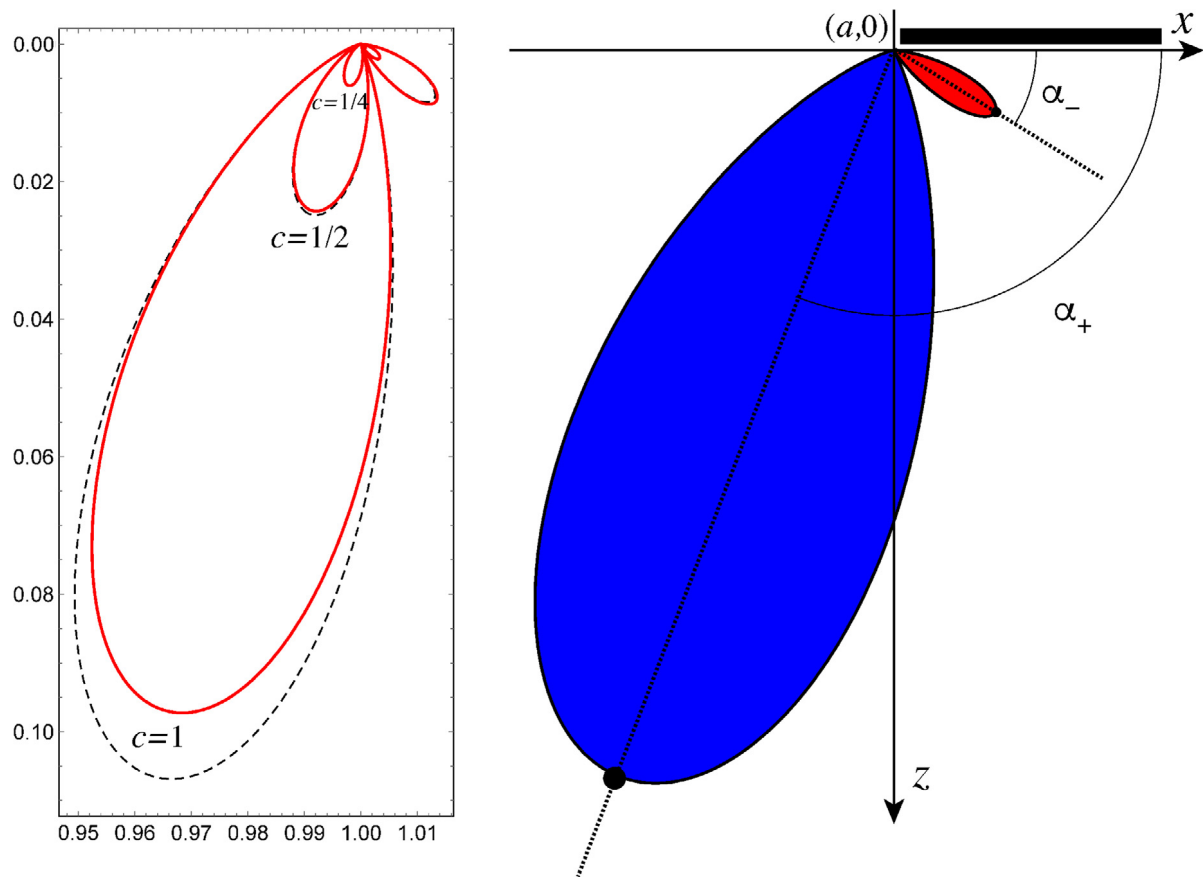


Fig. 10. Shape of the damage drops close to the edge and comparison between the approximation (red) and the actual damage drops (black) for $\tau_{crit} = E/2$. (For interpretation of the references to color in this figure legend, the reader is referred to the web version of this article.)

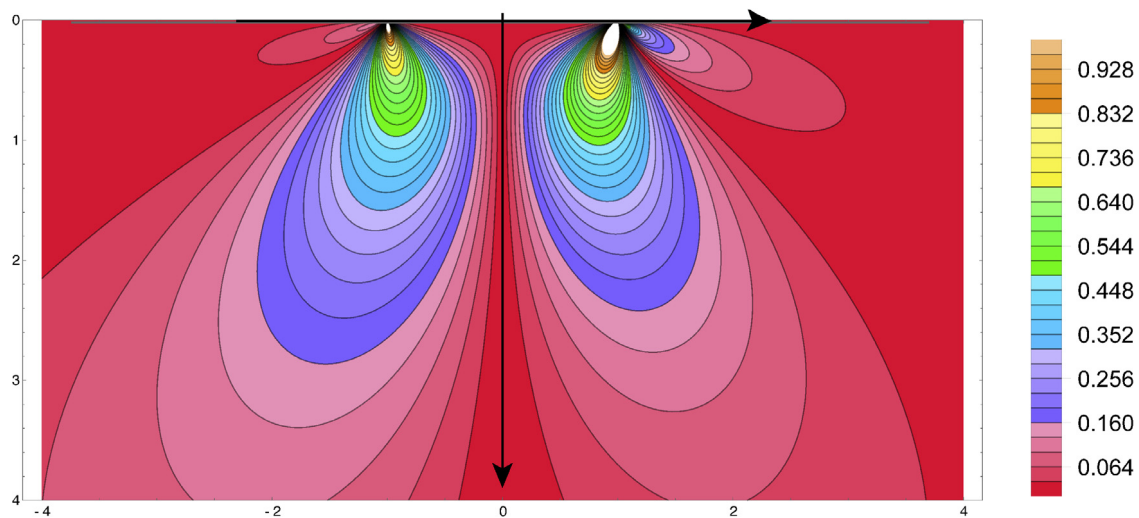


Fig. 11. Contour plot of the shear stress for $cE = 1$ in the sharp-edge case with the singularity placed at $b = 1$ (right) and in the curved-edge case for $a/b = 0.9$ and $R/b = 0.2$ (left).

2. Conclusion

We have investigated edge effects in material bulging. Our analysis reveals that smoothing the edges decreases shear stresses in the material and increase slightly the overall height of the bulge. Damage areas related to both shear stress and stretching still exist but they are greatly diminished as long as the radius of curvature of the edges is small enough.

The results presented in this paper were obtained in the context of *linear* elasticity. It is important to consider the limitations of such results as it is well appreciated that soft tissues can operate in large deformations where nonlinearities play an important role. At the theoretical level, the importance of nonlinear effects in contact mechanics has been investigated by various authors [19–23]. In particular, it is known [21] that a treatment in linear elasticity can generate self-penetration in the solution and anomalous behaviors (such as the profile

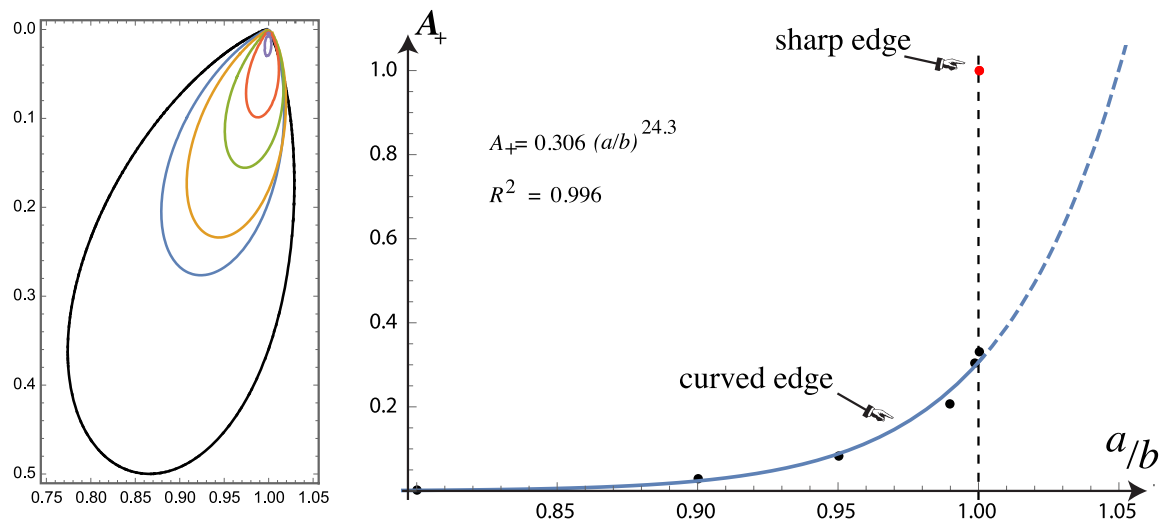


Fig. 12. Damage drops (left) and associated area A_+ (fitted with a power law) for $K = 1$ in the flat case (red dot online) and in the curved-edge case for $a/b \in \{0.8, 0.9, 0.95, 0.99, 0.99999\}$. (For interpretation of the references to color in this figure legend, the reader is referred to the web version of this article.)

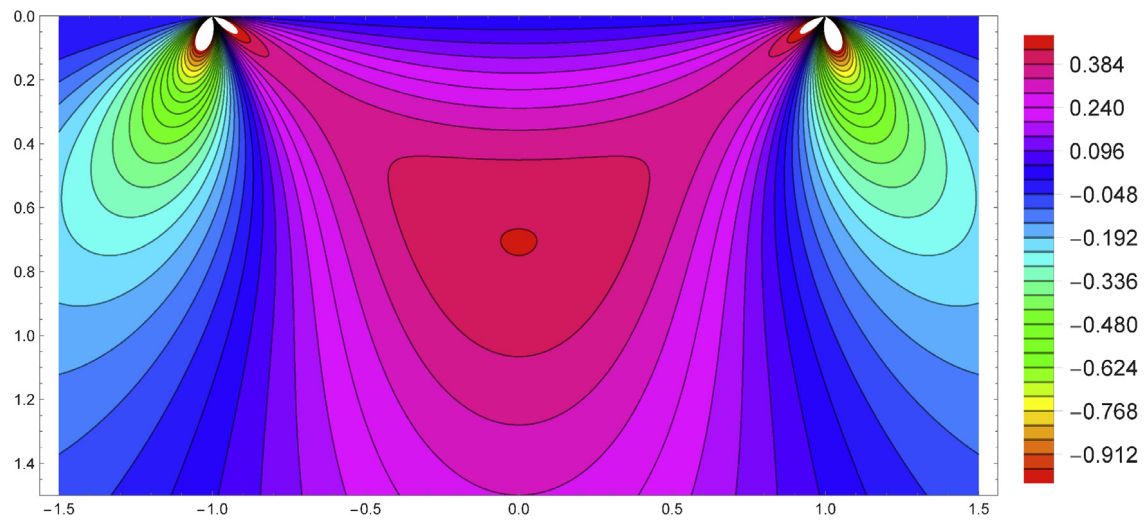


Fig. 13. Contour plot of the vertical strain for $v = 0.5$ and $c = 1.5$.

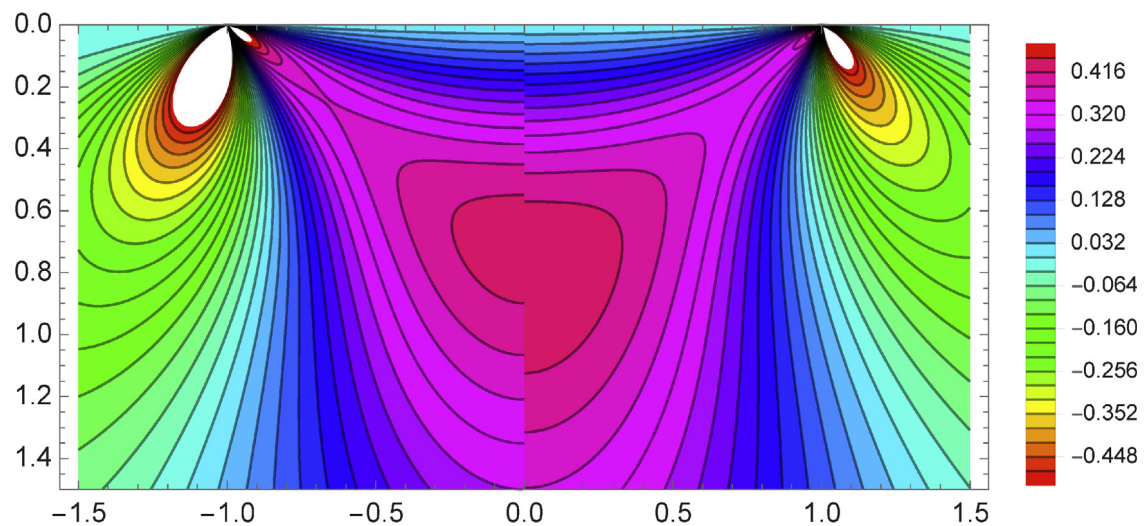


Fig. 14. Contour plot of the vertical strain for $v = 0.5$ and $c = 1.5$ in the sharp-edge case with the singularity placed at $b = 1$ (right) and in the curved-edge case for $a/b = 0.9$ and $R/b = 0.2$ (left).

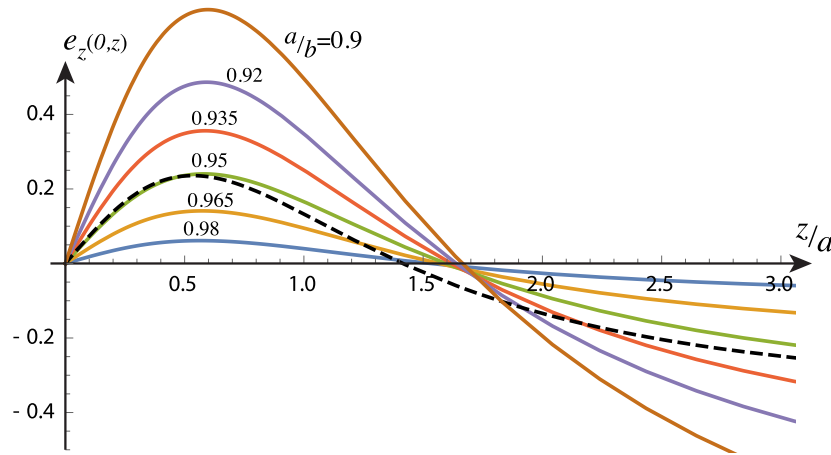


Fig. 15. Vertical strain for $\nu = 0.5$ and $c = 1.5$ in the sharp-edge case (black dashed) and in the curved-edge case for $a/b \in \{0.9, 0.92, 0.935, 0.95, 0.965, 0.98\}$ (smaller values lead to larger strains).

of the interface oscillating away from the contact). Yet, these effects seem to be concentrated close to the contact boundary whereas the profile away from it is mostly well described by the linear theory. The unreasonable effectiveness of the linear theory in Hertz-like problem is well known [24,25] but not yet understood. For our problem, in previous papers we have shown that the linear theory for bulging provides excellent agreement with finite-element simulations of non-linear materials in planar, cylindrical, and spherical geometries [5–7]. Here, we also provide experimental validations showing that the linear solution provides excellent predictions for displacement of the same order as the radius of the opening (See Fig. 7).

Going back to the original motivation, it should be clear that decompressive craniectomy is an extremely complex physiological process. Yet, basic physical ideas emerge from our highly idealized system and we expect our results concerning the shape of the bulge, the singularities of the stresses and the orientation of the damage drops to be generic for any type of bulging problem. Importantly, large stresses are generated at the opening, but, as shown here, these stresses can be partially mitigated by curved edges. However, Fletcher et al. [10] showed that in practice, the chaffer profile may not have much of an influence. A possible physical process to further mitigate these high stresses would be to employ a flexible toric joint that would extend the contact zone while providing some elasticity.

Acknowledgment

The support for Alain Goriely by the Engineering and Physical Sciences Research Council of Great Britain under research grant EP/R020205/1 is gratefully acknowledged.

Appendix A. The homogeneous solution to the singular integral equation

Consider the domain $S = (-\infty, -a] \cup [a, \infty)$ and an integrable function $f(x) : x \in S \rightarrow \mathbb{R}$. We are interested in finding the general solution to following singular integral equation with gap:

$$\left(\int_{-\infty}^{-a} + \int_a^{\infty} \right) \frac{p(s)}{x-s} ds = f(x), \quad |x| \geq a, \quad (\text{A.1})$$

We first look for homogeneous solutions when pressure p is either an even or odd function of x .

A.1. p even

If p is even, we can rewrite the integral in (A.1) as

$$\left(\int_{-\infty}^{-a} + \int_a^{\infty} \right) \frac{p(s)}{x-s} ds = \int_a^{\infty} p(s) \left(\frac{1}{x-s} + \frac{1}{x+s} \right) ds$$

$$= 2x \int_a^{\infty} \frac{p(s)}{x^2 - s^2} ds. \quad (\text{A.2})$$

Then the integral equation (A.1) is

$$\int_a^{\infty} \frac{p(s)}{x^2 - s^2} ds = \frac{f(x)}{2x}, \quad |x| \geq a. \quad (\text{A.3})$$

Following [26], we introduce new $x^2 = u$ and $s^2 = v$, so that (A.3) reads now

$$\int_a^{\infty} \frac{P(v)}{u-v} dv = F(u), \quad |u| \geq a^2, \quad (\text{A.4})$$

where

$$P(v) = \frac{p(\sqrt{v})}{\sqrt{v}} \quad \text{and} \quad F(u) = \frac{f(\sqrt{u})}{\sqrt{u}}. \quad (\text{A.5})$$

From [17], we find that the solution of (A.4) is given by

$$P(v) = \frac{c_0}{\sqrt{v-a^2}} + \frac{1}{\pi^2} \int_a^{\infty} \sqrt{\frac{u-a^2}{v-a^2}} \frac{F(u)}{u-v} du, \quad (\text{A.6})$$

where c_0 is a real constant. Hence the pressure is

$$p(s) = \frac{c_0 s}{\sqrt{s^2 - a^2}} + \frac{2s}{\pi^2} \int_a^{\infty} \sqrt{\frac{x^2 - a^2}{s^2 - a^2}} \frac{f(x)}{x^2 - s^2} dx, \quad s \geq a. \quad (\text{A.7})$$

In the case $f(x) = 0$, we extract from this last expression the even kernel

$$p_{\text{even}}(s) = \frac{c_0 |s|}{\sqrt{s^2 - a^2}}, \quad |s| \geq a. \quad (\text{A.8})$$

A.2. p odd

We enforce the condition that p is odd:

$$\begin{aligned} \left(\int_{-\infty}^{-a} + \int_a^{\infty} \right) \frac{p(s)}{x-s} ds &= \int_a^{\infty} p(s) \left(\frac{1}{x-s} - \frac{1}{x+s} \right) ds \\ &= - \int_a^{\infty} \frac{p(s)}{x^2 - s^2} 2s ds. \end{aligned} \quad (\text{A.9})$$

Then (A.1) is rewritten

$$\int_a^{\infty} \frac{p(s)}{x^2 - s^2} 2s ds = f(x), \quad |x| \geq a. \quad (\text{A.10})$$

Using the same transformation $x^2 = u$ and $s^2 = v$, (A.10) becomes

$$\int_a^{\infty} \frac{p(\sqrt{v})}{u-v} dv = f(\sqrt{u}), \quad |u| \geq a^2. \quad (\text{A.11})$$

Its solution is [17]:

$$p(\sqrt{v}) = \frac{c_1}{\sqrt{v-a^2}} + \frac{1}{\pi^2} \int_a^{\infty} \sqrt{\frac{u-a^2}{v-a^2}} \frac{f(\sqrt{u})}{u-v} du, \quad (\text{A.12})$$

where c_1 is a real constant. Hence the pressure is given by

$$p(s) = \frac{c_1}{\sqrt{s^2 - a^2}} + \frac{2}{\pi^2} \int_a^\infty \sqrt{\frac{x^2 - a^2}{s^2 - a^2}} \frac{xf(x)}{x^2 - s^2} dx, \quad s \geq a, \quad (\text{A.13})$$

from which we extract the odd homogeneous solution:

$$p_{\text{odd}}(s) = \frac{c_1 \operatorname{sgn}(s)}{\sqrt{s^2 - a^2}}, \quad |s| \geq a. \quad (\text{A.14})$$

Appendix B. Non-homogeneous solutions to the singular integral equations

The previous analysis provides a way to identify homogeneous solutions to the singular integral equations. Expressions (A.7) and (A.13) can also be used to find some non-homogeneous solutions. However, these expressions do not capture all solutions. In particular in the case of a curved edge, we notice that the non-homogeneous parts appearing in both expressions vanish identically. Thus we must solve equation (A.1) in a different way. Here, we use the following result from [17], valid for an inhomogeneous term defined on a finite domain of the form:

$$f(x) = \begin{cases} 0, & |x| \geq b \\ \frac{x-b}{AR}, & a \leq x \leq b \\ \frac{x+b}{AR}, & -b \leq x \leq -a, \end{cases} \quad (\text{B.1})$$

Then the pressure is

$$p(s) = \frac{\operatorname{sgn}(s)}{\pi^2 \sqrt{s^2 - a^2}} \left[c_1 + \left(\int_{-\infty}^{-a} + \int_a^\infty \right) \frac{f(t) \sqrt{t^2 - a^2} \operatorname{sgn}(t)}{t - s} dt \right] \\ = \frac{\operatorname{sgn}(s)}{\pi^2 AR \sqrt{s^2 - a^2}} \\ \times \left[c_1 + \underbrace{\int_{-b}^{-a} \frac{(-t-b) \sqrt{t^2 - a^2}}{t - s} dt + \int_a^b \frac{(t-b) \sqrt{t^2 - a^2}}{t - s} dt}_{=I(s)} \right], \quad (\text{B.2})$$

where we recognize the odd homogeneous solution. The explicit evaluation of this integral gives

$$I(s) = -\sqrt{s^2 - a^2} \left(s \ln \left| \frac{b^2 - 2a^2 + s^2 + 2\sqrt{(b^2 - a^2)(s^2 - a^2)}}{b^2 - s^2} \right| \right. \\ \left. + b \ln \left| \frac{b-s}{b+s} \frac{a^2 + bs - \sqrt{(b^2 - a^2)(s^2 - a^2)}}{a^2 - bs - \sqrt{(b^2 - a^2)(s^2 - a^2)}} \right| \right) \\ + 2s \left(\sqrt{b^2 - a^2} + b \ln \frac{a}{b + \sqrt{b^2 - a^2}} \right). \quad (\text{B.3})$$

When adding the even kernel, we obtain the general solution

$$p(s) \pi^2 AR = \frac{c_1 \operatorname{sgn}(s)}{\sqrt{s^2 - a^2}} + 2 \frac{|s|}{\sqrt{s^2 - a^2}} \left(c_0 + \sqrt{b^2 - a^2} + b \ln \frac{a}{b + \sqrt{b^2 - a^2}} \right) \\ - |s| \ln \left| \frac{b^2 - 2a^2 + s^2 + 2\sqrt{(b^2 - a^2)(s^2 - a^2)}}{b^2 - s^2} \right| \\ - b \operatorname{sgn}(s) \ln \left| \frac{b-s}{b+s} \frac{a^2 + bs - \sqrt{(b^2 - a^2)(s^2 - a^2)}}{a^2 - bs - \sqrt{(b^2 - a^2)(s^2 - a^2)}} \right|. \quad (\text{B.4})$$

Physically, we are looking for a non-divergent even solution. Therefore, we choose $c_1 = 0$ and c_0 such that $p(a) = p(-a)$ does not diverge:

$$c_0 + \sqrt{b^2 - a^2} + b \ln \frac{a}{b + \sqrt{b^2 - a^2}} = 0. \quad (\text{B.5})$$

Taken together, the solution for the pressure is

$$p(s) = -\frac{1}{\pi^2 AR} \left(|s| \ln \left| \frac{b^2 - 2a^2 + s^2 + 2\sqrt{(b^2 - a^2)(s^2 - a^2)}}{b^2 - s^2} \right| \right. \\ \left. + b \operatorname{sgn}(s) \ln \left| \frac{b-s}{b+s} \frac{a^2 + bs - \sqrt{(b^2 - a^2)(s^2 - a^2)}}{a^2 - bs - \sqrt{(b^2 - a^2)(s^2 - a^2)}} \right| \right). \quad (\text{B.6})$$

Appendix C. Experimental details

Bulging experiments were performed by compressing confined elastic solids using a plate with a circular aperture. The solid is confined on all faces except for a circular opening in the top plate. As the plate is displaced (axial compression) the solid is free to expand through the circular opening. Under this compression, the soft solid bulged through the aperture permitting measurement of the axisymmetric deformation profile.

The experimental sample, of $R = 45$ mm and $H = 20.5$ mm, was fabricated from poly-vinyl siloxane (Elite Double 8, Zhermack). The PVS sample was produced by mixing together a base polymer and crosslinker in a ratio of 9:1, which resulted in soft solid with Young's modulus $E = 40$ kPa and Poisson's ratio $\nu = 0.5$. After thorough mixing, and while still liquid, the sample was degassed in a vacuum chamber before being left to cure at room temperature inside a cylindrical container, of radius 45 mm and height 30 mm, with no lid. Prior to compressive testing the Young's modulus of the sample was measured by performing flat punch indentation experiments using a custom-built structural testing machine. The sample was positioned on a precision micro-balance (Pioneer PA64C Analytic Balance, Ohaus) and indented by a cylindrical indenter, of diameter $2r_i = 1.25$ mm, connected to a linear actuator (M228.10S, Physik Instrumente) and driven by a computer-controlled stepper motor. Simultaneous readings of both the mass, m , and indentation, δ_i , provided a stress-strain curve from which the Young's modulus, E , could be calculated via $F = 2r_i E^* \delta_i$, where $F = mg$, $E = E^*(1 - \nu^2)$ and ν is the Poisson's ratio of the material.

Confined inside the container, the soft solid was subject to axial compression by a circular plate of radius 44 mm with a circular aperture of radius $b = 15$ mm located at its center. To investigate the effect of edges on bulging, tests were performed with plates that had apertures with straight edges and apertures with a radii of curvature $R = 2$ mm and $R = 3$ mm. The plates, and the container that held the sample, were fabricated from ABS plastic using a 3D printer (MakerBot) with a resolution of 0.2 mm. The plate was attached to a computer-controlled linear actuator (M229.26S, Physik Instrumente) with a precision of ± 0.1 μm , that moved at 10 $\mu\text{m/s}$, applying an axial compression to the sample. Under compression, the soft solid bulged through the central aperture and the axisymmetric deformation profile was measured by imaging a line along the center of the sample. The line was approximately 1 mm wide, made from the same material, and with the same E , as the bulk and colored using an oil-based dye to contrast the rest of the sample. The line was imaged using a DSLR camera (D7000, Nikon), with a spatial resolution of 0.02 mm/pixel, positioned at 45 degrees to the horizontal and orthogonal to the line, at a rate of 1 fps. The line was detected in images using image processing techniques in Matlab, and compared to an undeformed reference line obtained for zero compression, resulting in measurements of the deformation profile accurate to 0.1 mm. The profiles shown in this paper were obtained for fixed values of axial compression in the range of 0.5 mm to 3.5 mm in 0.5 mm increments; in Fig. 7 for a curved-edge aperture of $R = 3$ mm.

Appendix D. Supplementary data

Supplementary material related to this article can be found online at <https://doi.org/10.1016/j.ijnonlinmec.2018.07.004>.

References

- [1] A. Marmarou, R.L. Anderson, J.D. Ward, S.C. Choi, H.F. Young, H.M. Eisenberg, M.A. Foulkes, L.F. Marshall, J.A. Jane, Impact of ICP instability and hypotension on outcome in patients with severe head trauma instability and hypotension on outcome in patients with severe head trauma, *J. Neurosurg.* (1991).
- [2] R.G. Ellenbogen, S.I. Abdulrauf, L.N. Sekhar, *Principles of Neurological Surgery*, Elsevier, Saunders, 2012.
- [3] J.F. Soustiel, G.E. Sviri, E. Mahamid, V. Shik, S. Abeshaus, M. Zaaroor, Cerebral blood flow and metabolism following decompressive craniectomy for control of increased intracranial pressure, *Neurosurgery* 67 (1) (2010) 65–72.

- [4] A. Goriely, M.G.D. Geers, G.A. Holzapfel, J. Jayamohan, A. Jérusalem, S. Sivaloganathan, W. Squier, J.A.W. van Dommelen, S.L. Waters, E. Kuhl, Mechanics of the brain: perspectives, challenges, and opportunities, *Biomech. Model. Mechanobiol.* 14 (2015) 931.
- [5] J. Weickenmeier, C. Butler, P.G. Young, A. Goriely, E. Kuhl, The mechanics of decompressive craniectomy: Personalized simulations, *Comput. Methods Appl. Mech. Engrg.* (2016).
- [6] J. Weickenmeier, E. Kuhl, A. Goriely, The mechanics of decompressive craniectomy: Bulging in idealized geometries, *J. Mech. Phys. Solids* (2016).
- [7] J. Weickenmeier, P. Saez, C.A.M. Butler, P.G. Young, A. Goriely, Ellen Kuhl, Bulging brains, *J. Elasticity* 129 (1–2) (2017) 197–212.
- [8] D.J. Cooper, J.V. Rosenfeld, L. Murray, Y.M. Arabi, A.R. Davies, P. D'Urso, T. Kossmann, J. Ponsford, I. Seppelt, P. Reilly, R. Wolfe, Decompressive craniectomy in diffuse traumatic brain injury, *New England J. Med.* 364 (16) (2011) 1493–1502.
- [9] A.G. Kolias, P.J. Kirkpatrick, P.J. Hutchinson, Decompressive craniectomy: past, present and future, *Nat. Rev. Neurol.* (2013).
- [10] Tim L. Fletcher, Barbara Wirthl, Angelos G. Kolias, Hadie Adams, Peter J.A. Hutchinson, Michael P.F. Sutcliffe, Modelling of brain deformation after decompressive craniectomy, *Ann. Biomed. Eng.* (2016) 1–15.
- [11] J.R. Barber, *Elasticity*, Springer, 1992.
- [12] A. Goriely, J. Weickenmeier, E. Kuhl, Stress singularities in swelling soft solids, *Phys. Rev. Lett.* 117 (13) (2016) 138001.
- [13] A. Goriely, *The Mathematics and Mechanics of Biological Growth*, Springer Verlag, New York, 2017.
- [14] V. Cerruti, Ricerche intorno all' equilibrio de'corpi elastici isotropi, *R. Accad. Lincei Mem. Cl. Sci. Fis. Mat. E Nat.* 3 (13) (1882) 81–122.
- [15] A. Flamant, Sur la répartition des pressions dans un solide rectangulaire chargé transversalement, *C. R. Acad. Sci. Paris* 114 (1892) 1465–1468.
- [16] D.J. Unger, Similarity solution of the flamant problem by means of a one-parameter group transformation, *J. Elasticity Phys. Sci. Solids* 66 (1) (2002) 93–97.
- [17] A. Chakrabarti, S.C. Martha, Methods of solution of singular integral equations, *Math. Sci.* 6 (1) (2012) 15.
- [18] K.L. Johnson, *Contact Mechanics*, Cambridge University Press, 1987.
- [19] Paul G. Warne, Debra A. Polignone, Solutions for an infinite compressible nonlinearly elastic body under a line load, *Quart. Appl. Math.* 54 (2) (1996) 317–326.
- [20] Adair Aguiar, Roger Fosdick, A singular problem in incompressible nonlinear elastostatics, *Math. Models Methods Appl. Sci.* 10 (08) (2000) 1181–1207.
- [21] Adair Aguiar, Roger Fosdick, Self-intersection in elasticity, *Int. J. Solids Struct.* 38 (28–29) (2001) 4797–4823.
- [22] Ethan T. Coon, Debra Polignone Warne, Paul G. Warne, Asymptotic analysis of finite deformation in a nonlinear transversely isotropic incompressible hyperelastic half-space subjected to a tensile point load, *J. Elasticity* 75 (3) (2004) 197–228.
- [23] V.M. Mal'kov, Yu.V. Mal'kova, Analysis of a stress singularity in a non-linear flamant problem for certain models of a material, *J. Appl. Math. Mech.* 72 (4) (2008) 468–474.
- [24] G.M. Pharr, W.C. Oliver, F.R. Brotzen, On the generality of the relationship among contact stiffness, contact area, and elastic modulus during indentation, *J. Mater. Res.* 7 (3) (1992) 613–617.
- [25] Andong He, John S. Wettlaufer, Hertz beyond belief, *Soft Matter* 10 (13) (2014) 2264–2269.
- [26] S. Banerjee, B.N. Mandal, Solution of a singular integral equation in a double interval arising in the theory of water waves, *Appl. Math. Lett.* (1993).